Supplementary Information

An excellent example illustrates the fluorescence sensing property of cobalt–organic framework

Chuan-Lei Zhang,[a,b] Zi-Teng Liu,[c] Heng Xu,[b] He-Gen Zheng[a], Jing Ma*[c], Jing Zhao*[a]*

a. State Key Laboratory of Coordination Chemistry, School of Chemistry and Chemical Engineering, Collaborative Innovation Center of Advanced Microstructures, Nanjing University, Nanjing 210023, P. R. China

b. Anhui Provincial Laboratory of Optoelectronic and Magnetism Functional Materials, School of Chemistry and Engineering, Anqing Normal University, Anqing 246011, China.

c. Theoretical and Computational Chemistry Institute, School of Chemistry and Chemical Engineering, Nanjing University, Nanjing 210093, China

Content

1. Experimental section.

Materials and measurements. Reagents and solvents employed were commercially available. Ligand TPY was prepared by the literature methods.[1] H_4L ligand was prepared on the basis of palladium-catalyzed cross-coupling reactions as follows. IR absorption spectrum of the compound **1** was recorded in the range of 400–4000 cm^{-1} on a Nicolet (Impact 410) spectrometer with KBr pellets (5 mg of sample in 500 mg of KBr). C, H and N analyses were carried out with a Perkin Elmer 240C elemental analyzer. Powder X-ray diffraction (PXRD) measurements were performed on a Bruker D8 Advance X-ray diffractometer using Mo-K_α radiation (λ = 0.71073 Å), in which the X-ray tube was operated at 40 kV and 40 mA. The as-synthesized samples were characterized by Thermogravimetry-Differential Scanning Calorimetry (TG-DSC) on a simultaneous thermal analyzer NETZSCH STA 449 F3 up to 1023 K using a heating rate of 10 K min^{-1} under N_2 atmosphere. Direct current (DC) magnetic susceptibility and magnetization measurements were carried out on a Quantum Design MPMS-XL7 superconducting quantum interference device (SQUID) magnetometer.

Photoluminescent Sensing Experiments. Finely ground sample of **1** (1 mg) was immersed in 3 mL H_2O, respectively, treated by ultrasonication for 2 h, and then aged for 24 h to form stable suspensions before the fluorescence study. The fluorescence was measured in-situ after incremental addition of freshly prepared 5 × 10^{-3} M $M(NO_3)_x$ (M= Mg^{2+}, Al^{3+}, Ca^{2+}, Cr^{3+}, Fe^{2+}, Fe^{3+}, Co^{2+}, Ni^{2+}, Cu^{2+}, Zn^{2+}, Cd^{2+} Eu^{3+}, Tb^{3+}) and HCl, NaOH solutions. The suspension was stirred at constant rate during experiment to maintain homogeneity.

Synthesis of H_4L. A mixture of 2,5-dibromo-p-xylene (10 mmol, 2.69 g), 4-methylphenylboronic acid (25 mmol, 3.40 g), K_2CO_3 (25 mmol, 3.45 g), and tetrakis(triphenylphosphine)palladium(0) (0.05 mmol, 2.20 mg) in mixed solvent of 90 mL 1,4-dioxane and 60 mL water was refluxed for 3 days under the atmosphere of nitrogen. The cooled solution was extracted with trichloromethane three times, and the organic solvent was evaporated. The crude product L-$(CH_3)_4$ was obtained from concentration under vacuum and purified by column chromatography (silica gel, ethylacetate/petroleum ether, 10 vol %). Yield: 80 %. Anal. (%): calc. for $C_8H_5BrO_4$: C, 92.26; H, 7.74. Found: C, 92.44; H, 7.81.

In a 250 ml flask, L-$(CH_3)_4$ (5 mmol, 1.43 g) and NaOH (40 mmol, 1.60 g) were dissolved in mixed solvent of 50 mL tert-Butanol and 50 mL water, the temperature of the mixture was controlled at 50 °C. Then, $KMnO_4$ (40 mmol, 6.32 g) was added to the solution five minutes per time. After that, the temperature was raised to 70 °C for 24 h. The solution was filtered, washed three times with 20 ml of water, and then concentrated to about 50 ml. The solution was acidified with concentrated hydrochloric acid and the product was collected by filtration (1.85 g, yield: 91 %). ^{1}H-NMR (600 MHz, DMSO-d): 13.23 (s, 1H), 13.06 (s, 1H), 8.02 (d, 2H), 7.79 (s, 1H), 7.55 (d, 2H).

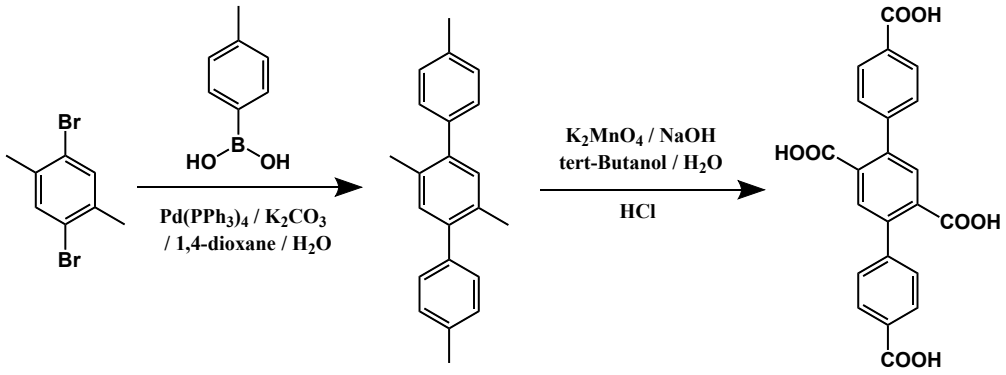

Scheme S1 Synthetic route of H_4L.

Synthesis of complex 1. A mixture of acetonitrile / H_2O (8 ml: 4 / 4) containing the H_4L (20.30 mg, 0.05 mmol), TPY (11.65 mg, 0.05 mmol) and $Co(NO_3)_2 \cdot 6H_2O$ (58.20 mg, 0.2 mmol) was mixed in a Teflon vessel within the autoclave. The vessel was heated at 95 °C for 72 h and then cooled to room temperature. Large quantities of crystals **1** were obtained and filtered off, washed with mother liquid, and dried under ambient conditions. Yield is 64 % based on H_4L. Elemental analysis calcd. for $C_{37}H_{27}CoN_3O_{10}$ (**1**): C, 60.61; H, 3.69; N, 5.73, Found: C, 60.82; H, 3.88; N, 5.64. The IR spectra of the corresponding compounds are shown in the Fig. S4-6.

X-ray crystallography. Single crystal X-ray diffraction measurement was carried out on a Bruker Apex Smart CCD diffractometer equipped with a Mo-Kα sealed-tube X-ray source (λ = 0.71073 Å, graphite monochromated). The data frames were recorded using the program APEX2 and processed using the program *SAINT* routine within APEX2.[2] The data were corrected for absorption based on the multi-scan technique as

implemented in *SADABS*.[3] The structures were solved by direct method using *SHELXS* and refined by full-matrix least-squares on F^2 using *SHELXTL* software.[4] Crystallographic data for the structure reported in this paper have been deposited in the Cambridge Crystallographic Data Center with CCDC Number 1559997 for **1**. Relevant parameters are given in Table S1. Selected bond lengths and angles are listed in Table S2. Hydrogen-Bonding geomentry is listed in Table S3.

Table S1. Crystal data and structural refinements parameters of complex **1**.

complex	**1**
Empirical formula	$C_{37}H_{27}CoN_3O_{10}$
Formula weight	732.54
Crystal system	Monoclinic
Space group	$P\,2_1/c$
a / Å	12.545(3)
b / Å	15.163(4)
c / Å	18.579(4)
α / °	90
β/ °	115.029(14)
γ/ °	90
V / Å^3	3202.2(14)
Z	4
D_{calcd} / g cm^{-3}	1.519
μ / mm^{-1}	0.604
F(000)	1508
θ min-max / °	1.792, 28.379

Tot., uniq. data	22900, 7997
R(int)	0.0822
Nres, Npar	18, 462
R_1, wR_2 [$I > 2\sigma(I)$]	0.0570, 0.1386
GOF on F^2	1.010
Min. and max resd dens (e·Å^{-3})	-0.777, 0.676

Table S2. Selected Bond Lengths (Å) and Angles (deg) for complex **1**.

complex **1**			
Co1-O(1)	1.992(2)	Co1-O(9)#1	2.041(2)
Co1-O(8)#2	2.055(2)	Co1-N(1)	2.096(2)
Co1-O(3)	2.212(2)	Co1-O(3)#3	2.293(2)
O(1)-Co1-O(9)#1	108.42(9)	O(1)-Co1-O(8)#2	89.27(9)
O(1)-Co1-O(3)	169.08(8)	O(8)#2-Co1-N(1)	101.16(9)
O(8)#2-Co1-O(3)	80.49(8)	O(9)#1-Co1-O(3)	80.45(8)
O(1)-Co1-O(3)#3	81.15(8)	N(1)-Co1-O(3)	87.34(9)
O(8)#2-Co1-O(3)#3	87.01(8)	O(9)#1-Co1-O(3)#3	80.32(8)
N(1)-Co1-O(3)#3	171.82(9)	O(3)-Co1-O(3)#3	94.43(8)
O(9)#1-Co1-N(1)	92.13(9)	O(1)-Co1-N(1)	98.45(9)
O(9)#1-Co1-O(8)#2	156.15(8)		

Symmetry Codes for **1:** #1 = $x, -y + 1/2, z + 1/2$; #2 = $-x + 2, y - 1/2, -z + 1/2$; #3 = $-x + 2, -y, -z + 1$.

Table S3. Hydrogen-Bonding Geometry (Å, °) for **1**.

D−H···A	d(H···A)	d(D···A)	∠D−H···A
O1W−H1WB···O5	1.80	2.598(6)	156
O3−H3A···N2	1.81	2.754(4)	163

O3−H3B···O1W	1.92	2.741(4)	141
O4−H4···N3	1.92	2.617(5)	143
O7−H7···O2	1.85	2.665(4)	170

2. PXRD pattern, IR spectrum and TG-DSC curve.

From the PXRD pattern (Fig. S3), the peak positions of complex **1** are agree well with their simulated ones, indicating that the products have been successfully obtained as pure crystalline phases. IR of H_4L ligand (KBr, cm^{-1}): 2973w, 1922w, 1687w, 1198s, 1512m, 1437s, 1419s, 1256w, 1227vs, 1198vs, 1085m, 1019w, 849vs, 750vs, , 612vs, 482s (Fig. S4); IR of TPY ligand (KBr, cm^{-1}): 3028m, 1603s, 1549w, 1403vs, 1328w, 1223w, 1026w, 993w, 910w, 815vs, 710s, 625s, 544vs; IR of **1** (KBr, cm^{-1}): 3064w, 1719vs, 1685w, 1610vs, 1564vs, 1417vs, 1349s, 1228s, 1177m, 1120m, 1015s, 865s, 835s, 776m, 709s, 644s, 581m, 547s. (Fig. S4-S6)

In order to characterize the thermal stability of **1**, thermogravimetry-differential scanning calorimetry (TG-DSC) analysis was studied in detail. From the TG-DSC diagram (Fig. S7), the weightlessness 2.46% for **1** is equivalent to losing one lattice H_2O molecule (calcd 2.60%) before 200 °C, meanwhile, an endothermic peak appears on the DSC curve. Then the curve presents a gravity platform until 330 °C. The DSC curve shows a large endothermic peak, the TG curve decreases significantly, which suggests that the hydrogen bonding interaction in the crystal lattice is destroyed, and the host skeleton begin to collapse. Thereafter, the components of the sample lose further, and another endothermic peak appeares in the DSC curve.

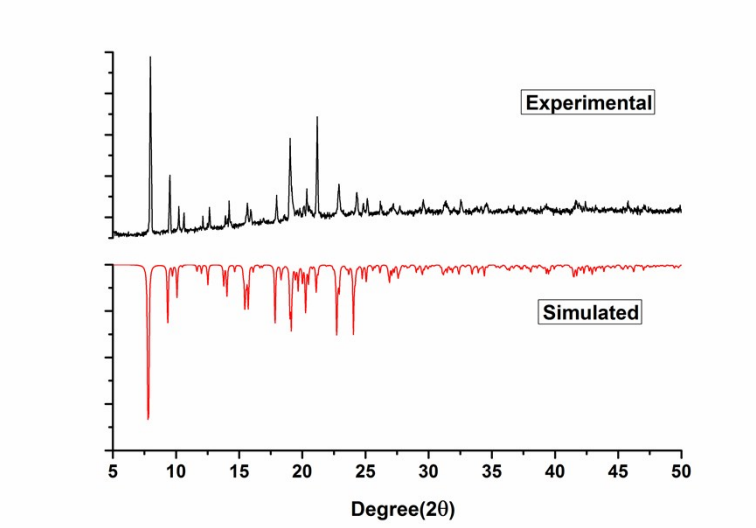

Fig. S1 Powder X-ray diffraction patterns of complex **1**.

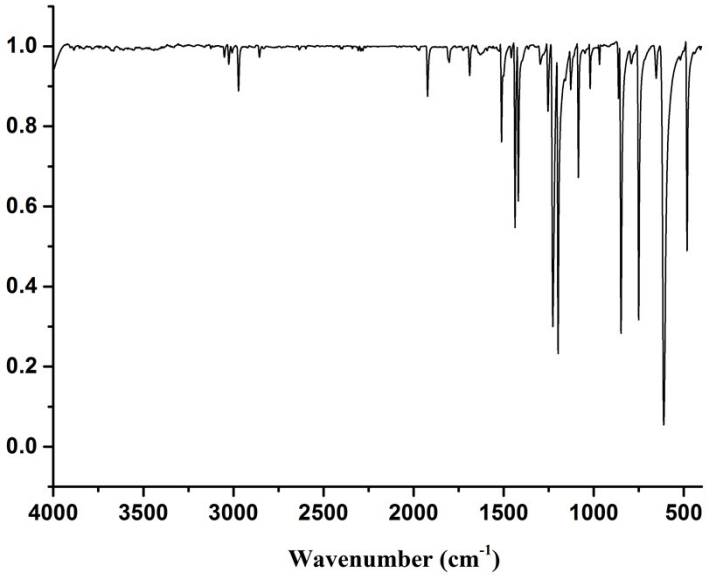

Fig. S2 IR spectra of H_4L ligand.

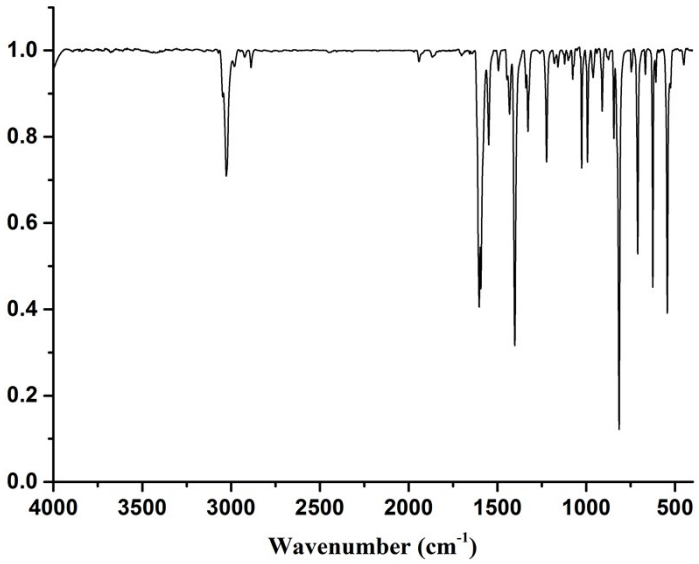

Fig. S3 IR spectra of TPY ligand.

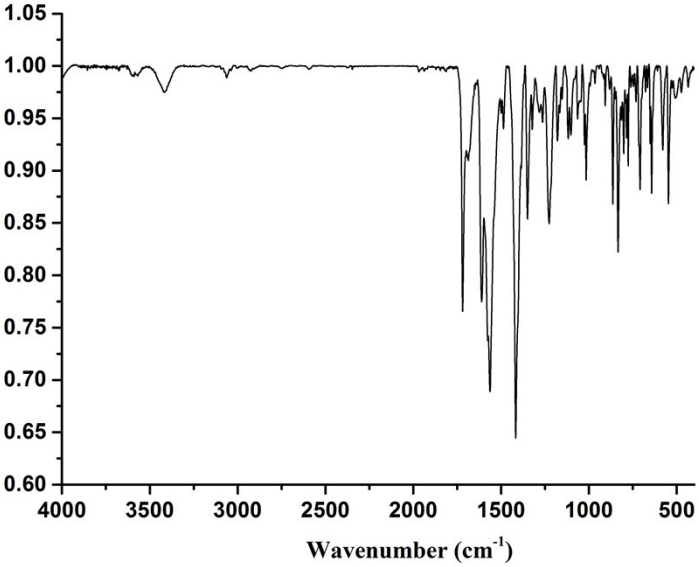

Fig. S4 IR spectra of complex **1**.

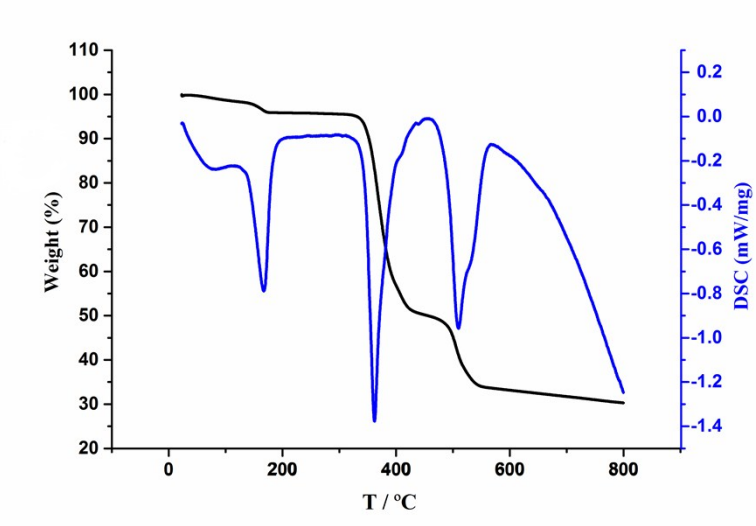

Fig. S5 TG-DSC curve of complex **1**.

3. Magnetic property and computational methods of 1.

Magnetic property. The general spin Hamiltonian applied for centrosymmetric dinuclear Co^{II} complex **1**:

$$\hat{H} = g\beta(\hat{S}_1 + \hat{S}_2)\cdot B + \hat{S}_1\cdot D_1\cdot\hat{S}_1 + \hat{S}_2\cdot D_2\cdot\hat{S}_2 - J\,\hat{S}_1\cdot\hat{S}_2 \quad (1)$$

The good fit of the data is: J = 1.48 cm^{-1} , $g_1 = g_2$ = 1.71 , $D_1 = D_2$ =43.6 cm^{-1} , $E_1 = E_2$ = 6.75 cm^{-1}.

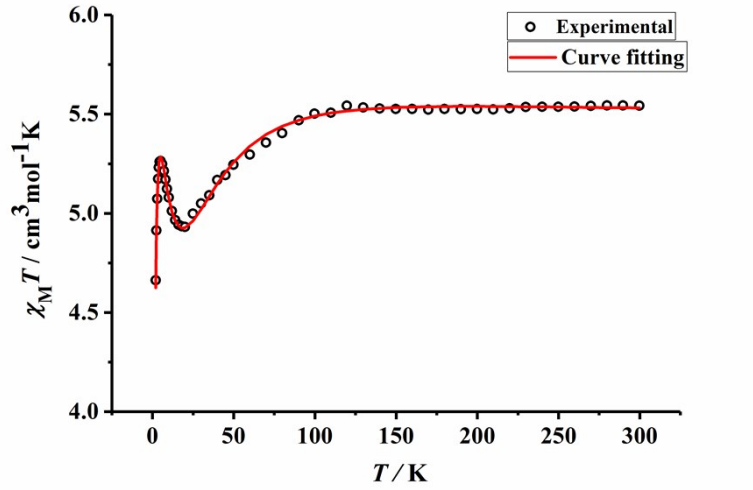

Fig. S6 Temperature dependence of the $\chi_M T$ product for **1**.

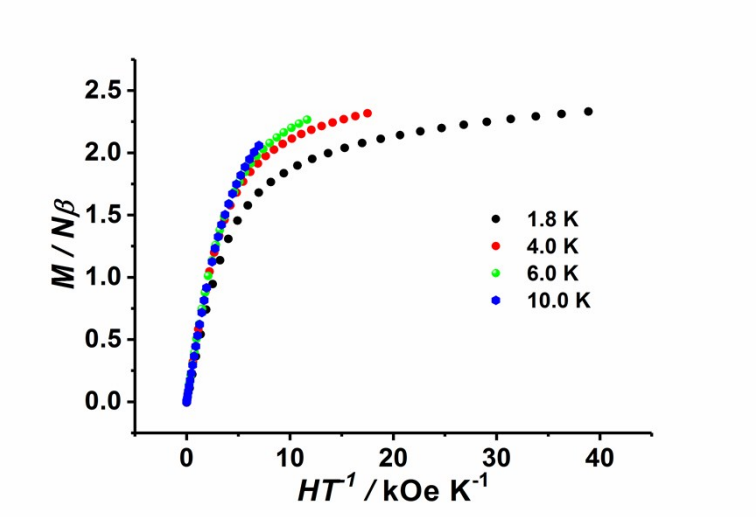

Fig. S7 Field-dependent magnetization measurement at the indicated temperatures for **1**.

Computational methods. All the calculations were performed in the program package Gaussian16.[5] The single point energy calculation of complex **1** and optimizations of ligands were carried out at Density Functional Theory (DFT) M06-2X [6] level. For nonmetal elements, the standard 6-311G(d) basis sets were used and for the metal Co, we used the effective core potentials (ECPs) with double-ζ valence basis sets (LanL2DZ).[7] Structure of complex **1** was taken from crystal structure. The Self-consistent field convergence criterion was set to 10^{-5}.

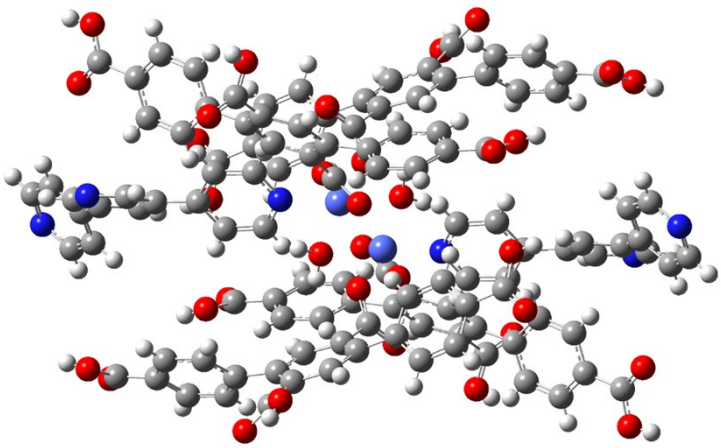

Fig. S8 The DFT computational model of **1**.

Table S4. Comparison of the single point energies of complex **1** with different spin multiplicities with M06-2X functional.

Basis Set		Charge	Spin Multiplicity	Basis Functions	Energy/a.u.
Metal	Non-Metal		2S+1		
lanl2dz	6-311g(d)	0	1	3122	-7717.37776
lanl2dz	6-311g(d)	0	3	3122	-7717.53913
lanl2dz	6-311g(d)	0	5	3122	-7717.60033
lanl2dz	6-311g(d)	0	7	3122	-7717.66241

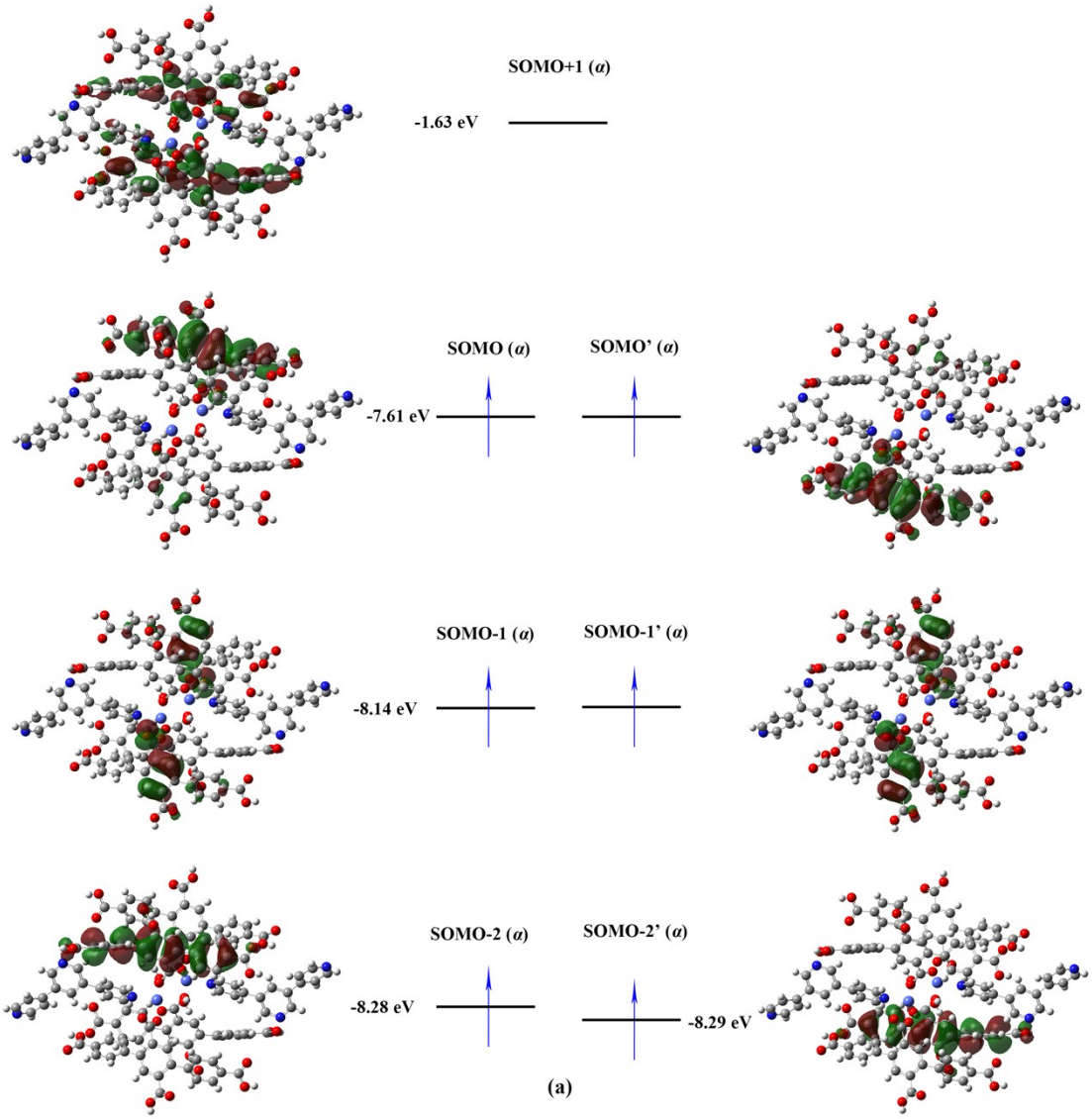

(a)

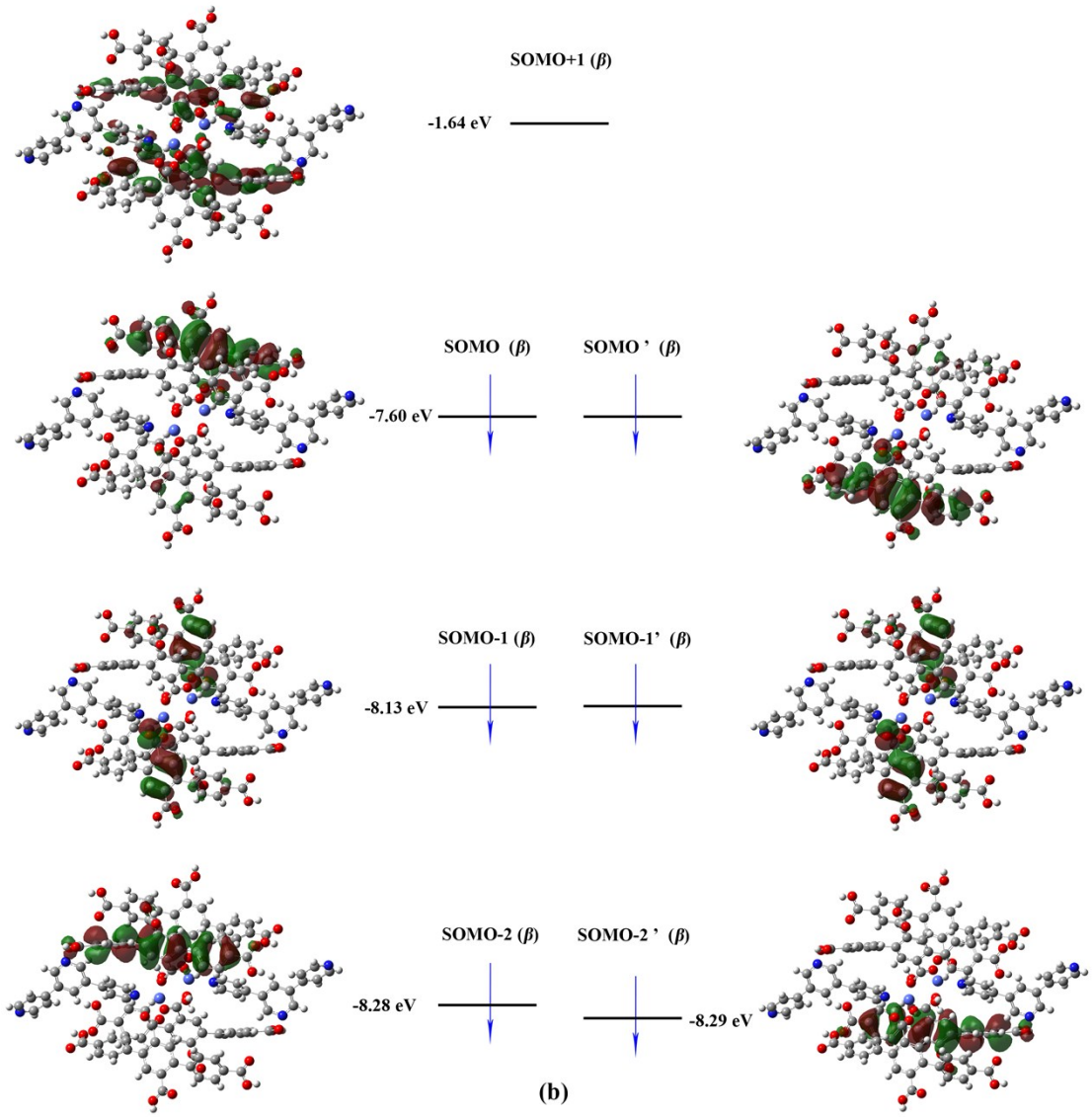

Fig. S9 Frontier molecular orbitals as well as their orbital energies calculated with M06-2X functional for complex **1**: (a) the α spin orbitals; (b) the β spin orbitals. Multiplicity = 7, $\langle S^2 \rangle$ = 12.02, E = -7717.66241 a.u.

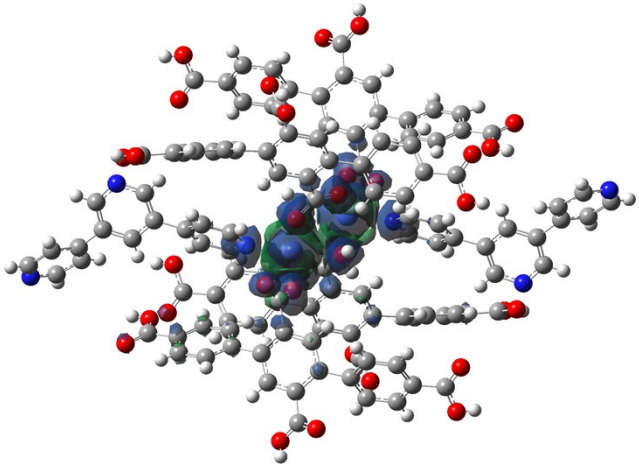

Fig. S10 Spin Density of complex **1** calculated with M06-2X functional.

The computational strategies for binding energy are given as follows:

$$E_{\text{Binding energy}} = E_{\text{Complex 1}} - (2 \times E_{\text{TPY}} + 4 \times E_{\text{H}_4\text{L}} + 2 \times E_{\text{H}_2\text{O}} + 2 \times E_{\text{Co}})$$

$$= -237.23 \text{ kcal / mol} \qquad (2)$$

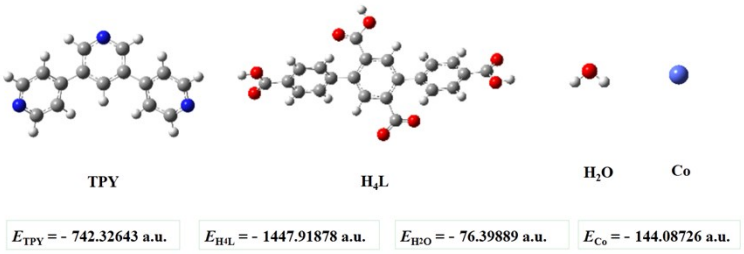

Fig. S11 The computational strategies for binding energy.

4. Excitation and emission spectra of 1.

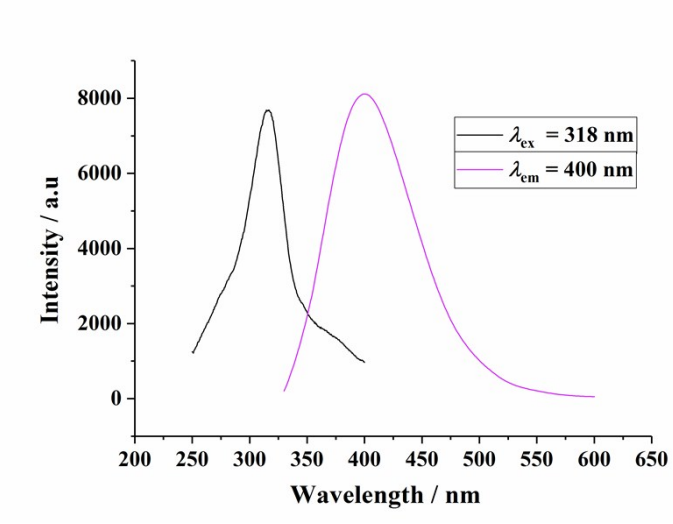

Fig. S12 Excitation (black, λ_{ex} = 318 nm) and emission spectra (purple, λ_{ex} = 400 nm) of **1**.

5. The changes of the luminescence intensity upon the addition of analytes.

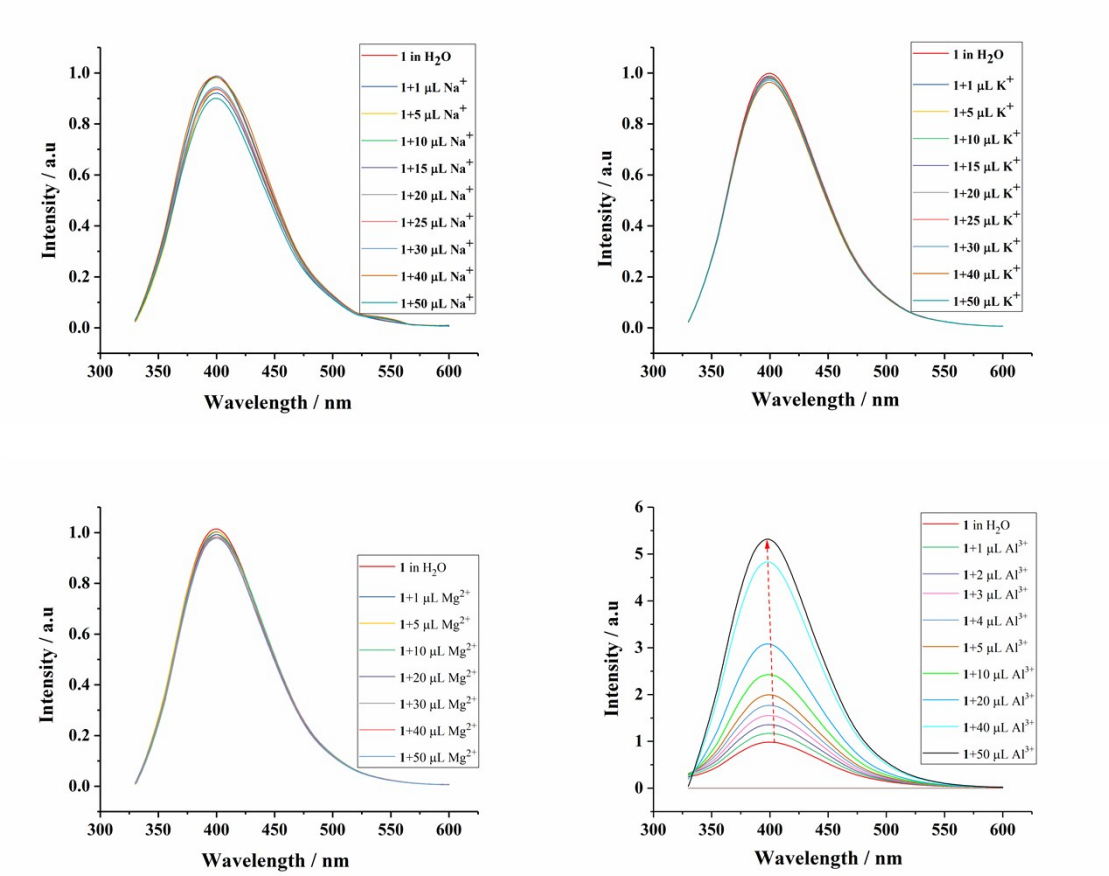

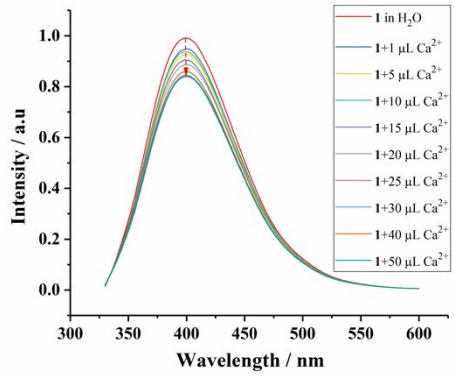
Intensity / a.u
Wavelength / nm
1 in H2O
1+1 μL Ca2+
1+5 μL Ca2+
1+10 μL Ca2+
1+15 μL Ca2+
1+20 μL Ca2+
1+25 μL Ca2+
1+30 μL Ca2+
1+40 μL Ca2+
1+50 μL Ca2+

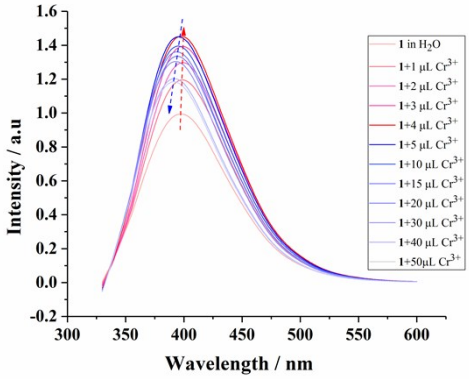
Intensity / a.u
Wavelength / nm
1 in H2O
1+1 μL Cr3+
1+2 μL Cr3+
1+3 μL Cr3+
1+4 μL Cr3+
1+5 μL Cr3+
1+10 μL Cr3+
1+15 μL Cr3+
1+20 μL Cr3+
1+30 μL Cr3+
1+40 μL Cr3+
1+50μL Cr3+

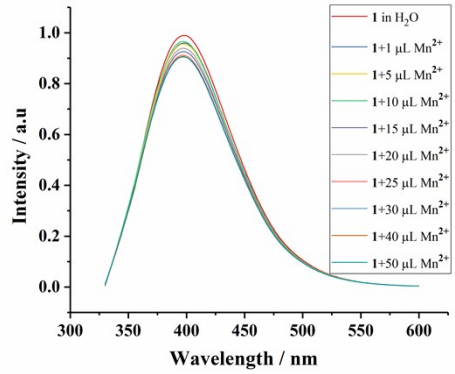
Intensity / a.u
Wavelength / nm
1 in H2O
1+1 μL Mn2+
1+5 μL Mn2+
1+10 μL Mn2+
1+15 μL Mn2+
1+20 μL Mn2+
1+25 μL Mn2+
1+30 μL Mn2+
1+40 μL Mn2+
1+50 μL Mn2+

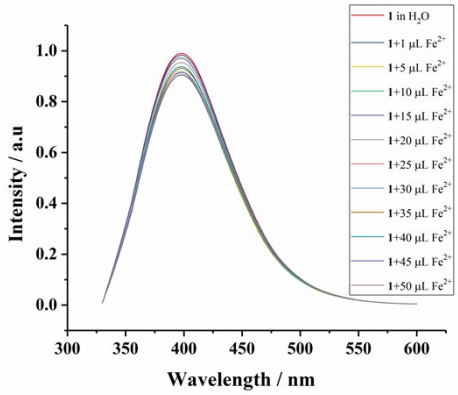
Intensity / a.u
Wavelength / nm
1 in H2O
1+1 μL Fe2+
1+5 μL Fe2+
1+10 μL Fe2+
1+15 μL Fe2+
1+20 μL Fe2+
1+25 μL Fe2+
1+30 μL Fe2+
1+35 μL Fe2+
1+40 μL Fe2+
1+45 μL Fe2+
1+50 μL Fe2+

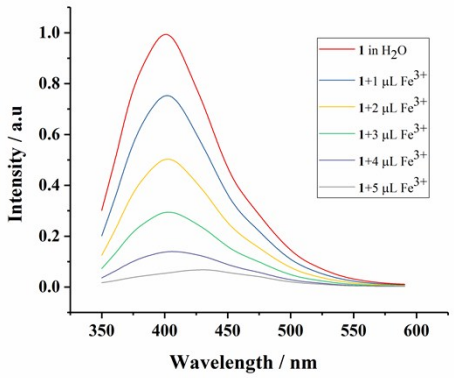
Intensity / a.u
Wavelength / nm
1 in H2O
1+1 μL Fe3+
1+2 μL Fe3+
1+3 μL Fe3+
1+4 μL Fe3+
1+5 μL Fe3+

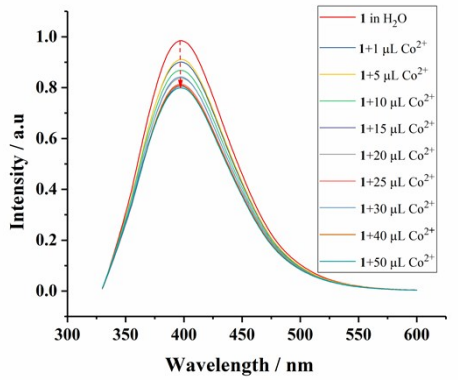
Intensity / a.u
Wavelength / nm
1 in H2O
1+1 μL Co2+
1+5 μL Co2+
1+10 μL Co2+
1+15 μL Co2+
1+20 μL Co2+
1+25 μL Co2+
1+30 μL Co2+
1+40 μL Co2+
1+50 μL Co2+

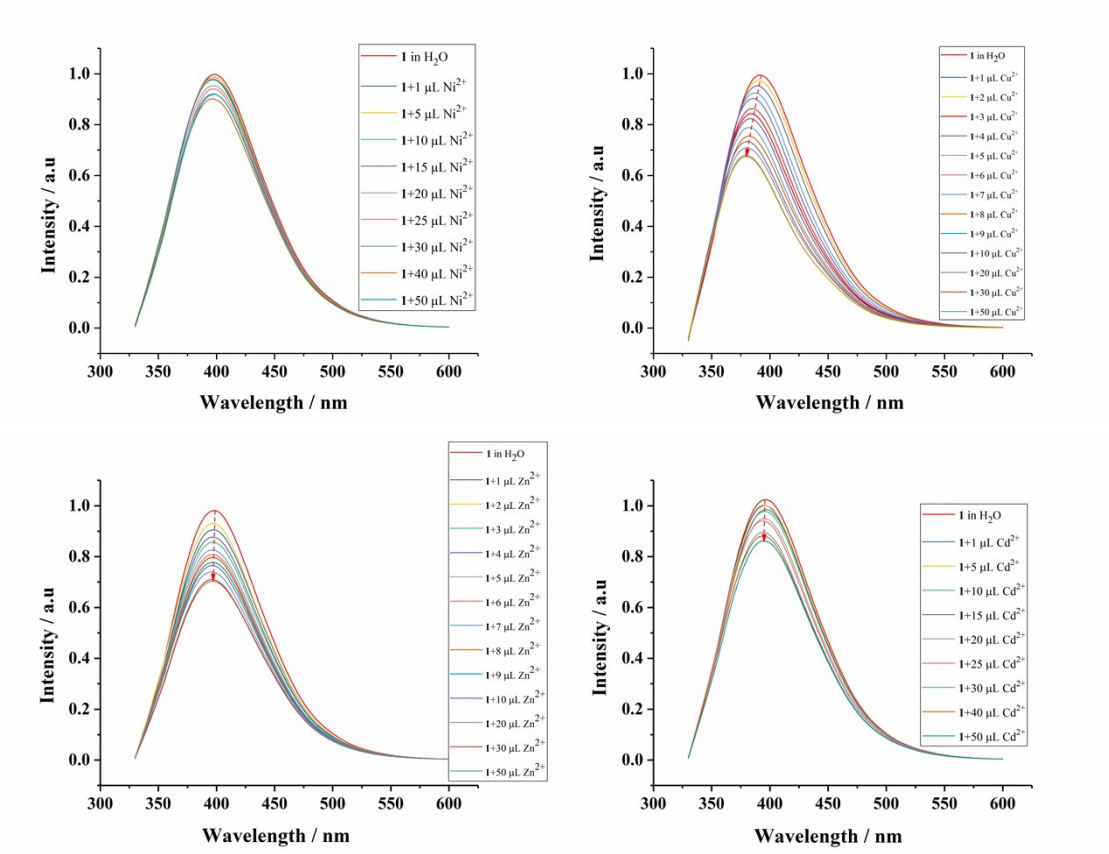

Fig. S13 Photoluminescence spectra of **1** by gradual addition different metal ions.

6. The detection limit for Al^{3+} at low concentrations.

Detection limit was determined according to the following definitions:

$$s_b = \sqrt{\frac{\sum_{i=1}^{n}(x_i - \bar{x})^2}{n-1}}$$

$$S = \frac{\Delta I}{\Delta c}$$

$$DL = \frac{3s_b}{S}$$

S is the slope of the calibration curve; s_b is the standard deviation for replicating detections of blank solutions.[8]

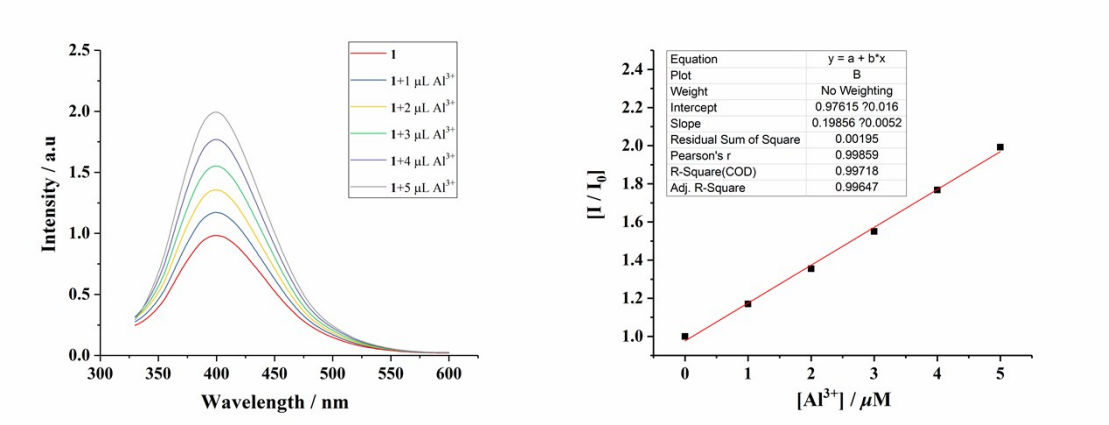

Fig. S14: left) Emission spectra of **1** dispersed in water upon incremental addition of water solution of Al^{3+} ions at low concentrations (λ_{ex} = 318 nm); right) The fitting curve of the emission intensity (at 400 nm) of **1** *vs*. concentration of Al^{3+} ions (where I_0 and I are luminescence intensity in absence and presence of Al^{3+} ions, respectively). Final concentration of Al^{3+} ions in the medium is indicated in the legend in μM unit.

Linear Equation: $y = 0.19856\,x + 0.97615$ $\quad R^2 = 0.99647$

$S = 1.9856 \times 10^5\ M^{-1}$

$s_b = 0.1105$ (n = 8)

$DL = 3\ s_b / S = 1.67 \times 10^{-6}$ M = 1.67 μM

7. The XPS results before and after titration of metal ions in 1.

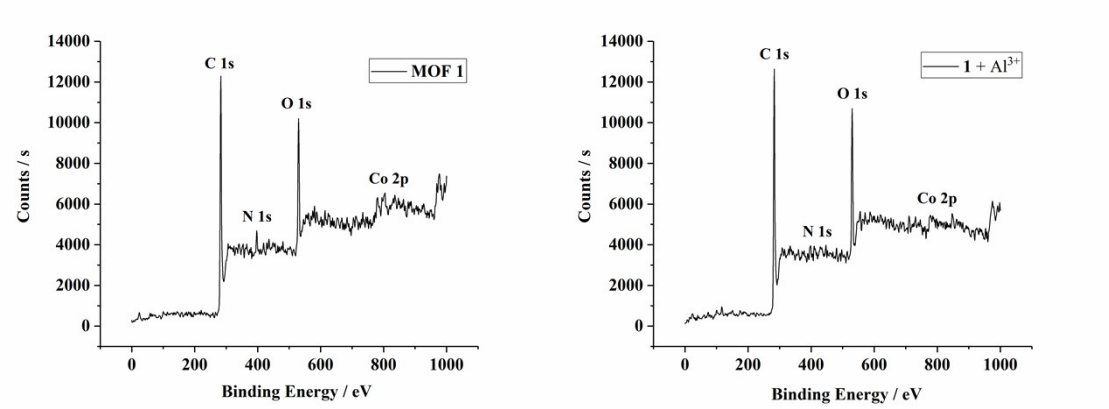

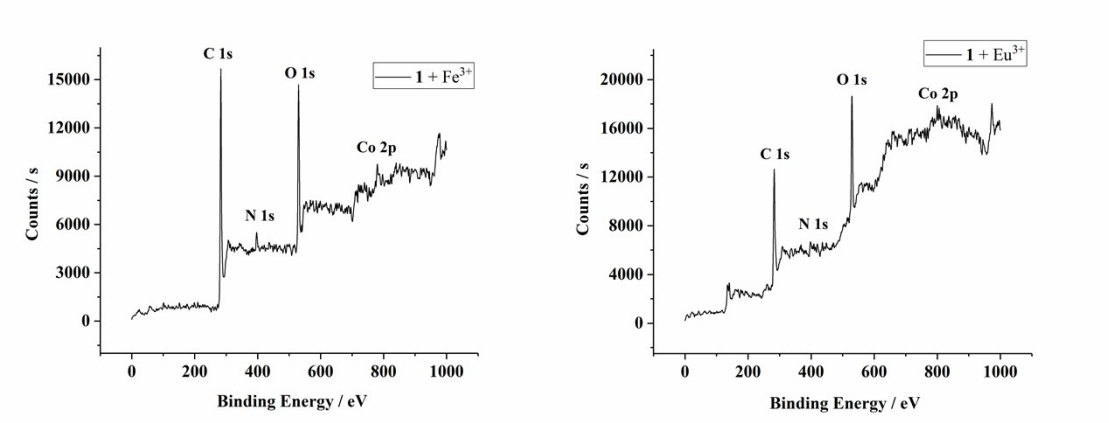

Fig. S15 Survey XPS spectra of **1** after immersed in Al^{3+}, Fe^{3+} and Eu^{3+}.

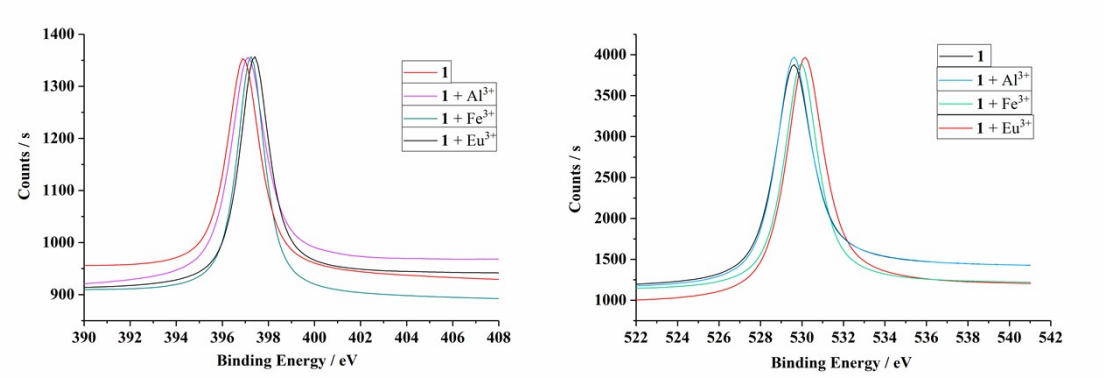

Fig. S16 N 1s (left) and O 1s (right) XPS spectra of **1** before and after immersed in Al^{3+}, Fe^{3+} and Eu^{3+}.

8. UV-vis absorption spectra of metal ions and 1 in aqueous solutions.

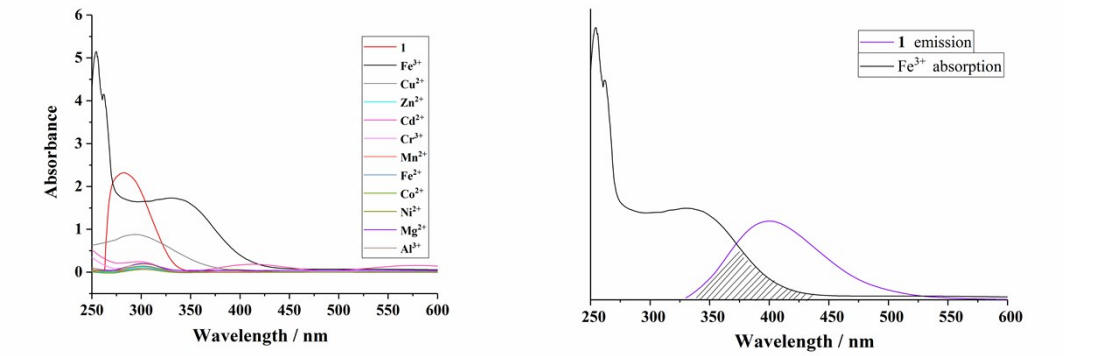

Fig. S17 left) Liquid UV−vis spectra of **1** and different metal ions; right) the overlap between the absorption spectrum of Fe^{3+} ions and the emission spectrum of **1**.

9. The results of titration of HCl/NaOH and Eu^{3+}/Tb^{3+}.

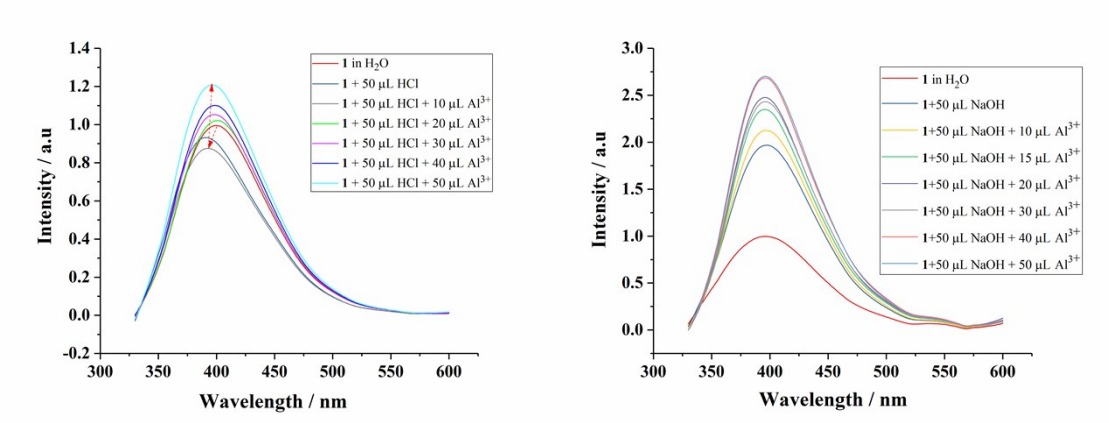

Fig. S18 left) Emission spectra of **1** dispersed in water upon addition of 50 μL (5×10^{-3} M) HCl solution, and then incremental addition of 5×10^{-3} M Al^{3+} solution; right) Emission spectra of **1** dispersed in water upon addition of 50 μL (5×10^{-3} M) NaOH solution, and then incremental addition of 5×10^{-3} M Al^{3+} solution.

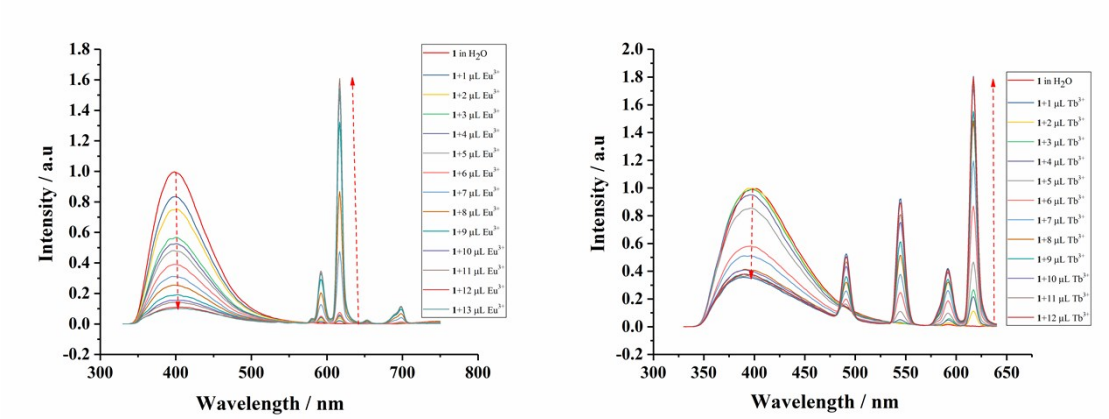

Fig. S19 left) Emission spectra of **1** dispersed in water upon incremental addition of 5×10^{-3} M Eu^{3+} solution; right) Emission spectra of **1** dispersed in water upon incremental addition of 5×10^{-3} M Tb^{3+} solution.

10. The selectivity detection for Al^{3+} ions in the presence of Fe^{3+} ions.

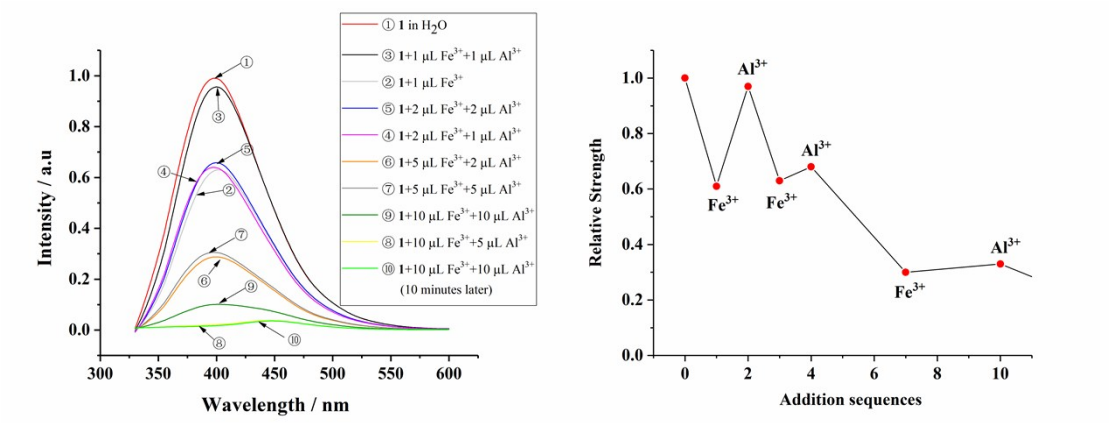

Fig. S20 left) Emission spectra of **1** dispersed in water upon cross-drop Fe^{3+} and Al^{3+}; right) changes in percentage of luminescence intensity of **1** upon the addition of water solution of Fe^{3+} ions followed by Al^{3+} ions.

References

1. Y. Kubota, K. Biradha, M. Fujita, S. Sakamoto and K. Yamaguchi, *Bull. Chem. Soc. Jpn.*, 2002, **75**, 559.
2. SAINT, Version 6.02; Bruker AXS: Madison, WI, 1999.
3. G. M. Sheldrick, SADABS: Empirical Absorption Correction-Program; University of Göttingen: Göttingen, Germany, 1997.
4. G. M. Sheldrick, SHELXTL Reference Manual, Version 6.10; Bruker AXS: Madison, WI, 2000.
5. Gaussian 16, Revision A.03, M. J. Frisch, G. W. Trucks, H. B. Schlegel, G. E. Scuseria, M. A. Robb, J. R. Cheeseman, G. Scalmani, V. Barone, G. A. Petersson, H. Nakatsuji, X. Li, M. Caricato, A. V. Marenich, J. Bloino, B. G. Janesko, R. Gomperts, B. Mennucci, H. P. Hratchian, J. V. Ortiz, A. F. Izmaylov, J. L. Sonnenberg, D. Williams-Young, F. Ding, F. Lipparini, F. Egidi, J. Goings, B. Peng, A. Petrone, T. Henderson, D. Ranasinghe, V. G. Zakrzewski, J. Gao, N. Rega, G. Zheng, W. Liang, M. Hada, M. Ehara, K. Toyota, R. Fukuda, J. Hasegawa, M. Ishida, T. Nakajima, Y. Honda, O. Kitao, H. Nakai, T. Vreven, K. Throssell, J. A. Montgomery, Jr., J. E. Peralta, F. Ogliaro, M. J. Bearpark, J. J. Heyd, E. N. Brothers, K. N. Kudin, V. N. Staroverov, T. A. Keith, R. Kobayashi, J. Normand, K. Raghavachari, A. P. Rendell, J. C. Burant, S. S. Iyengar, J. Tomasi, M. Cossi, J. M. Millam, M. Klene, C. Adamo, R. Cammi, J. W. Ochterski, R. L. Martin, K. Morokuma, O. Farkas, J. B. Foresman and D. J. Fox, Gaussian, Inc., Wallingford CT, 2016, **9**.
6. Y. Zhao and D. G. Truhlar, *Theor. Chem. Acc.* 2008, **120**, 215.
7. (a) P. J. Hay and W. R. J. Wadt, *Chem. Phys.* 1985, **82**, 270; (b) W. R. Wadt and P. J. Hay, *J. Chem. Phys.* 1985, **82**, 284; (c) P. J. Hay and W. R. Wadt, *J. Chem. Phys.* 1985, **82**, 299.
8. H. Xu, J. Gao, X. Qian, J. Wang, H. He, Y. Cui, Y. Yang, Z. Wang and G. Qian, *J. Mater. Chem. A.*, 2016, **4**, 10900.